Soft Matter

COMMUNICATION

View Article Online
View Journal

Check for updates

Cite this: DOI: 10.1039/d0sm00943a

Received 20th May 2020,
Accepted 16th September 2020

DOI: 10.1039/d0sm00943a

rsc.li/soft-matter-journal

Fluctuation spectroscopy of giant unilamellar vesicles using confocal and phase contrast microscopy†

Hammad A. Faizi,[ab] Cody J. Reeves,[c] Vasil N. Georgiev,[b] Petia M. Vlahovska *[ac] and Rumiana Dimova *[b]

A widely used method to measure the bending rigidity of bilayer membranes is fluctuation spectroscopy, which analyses the thermally-driven membrane undulations of giant unilamellar vesicles recorded with either phase-contrast or confocal microscopy. Here, we analyze the fluctuations of the same vesicle using both techniques and obtain consistent values for the bending modulus. We discuss the factors that may lead to discrepancies.

Bending rigidity of cellular membranes plays a key role in membrane remodeling. Knowledge of its value is needed to quantify processes that involve curvature changes such as budding (as in endo- and exocytosis), tubulation and fusion. Various experimental methods have been devised to measure bending rigidity,[1] *e.g.* micropipette aspiration,[2,3] electrodeformation,[4–7] optical tweezers,[8,9] and scattering based techniques.[10,11] One of the most popular methods is fluctuation spectroscopy, pioneered by Brochard and Lenon,[12] due to its ease of implementation.[6,13–15] In essence, a time series of vesicle contours in the focal plane (the equator of the quasi-spherical vesicle) is recorded. The quasi-circular contour is decomposed in Fourier modes. The fluctuating amplitudes have variance dependent on the membrane bending rigidity and tension. Imaging is most commonly done by phase contrast microscopy[1,6,14,16–21] but other methods such as confocal[22–24] and light sheet microscopy[25] have also been employed. The increased variety of imaging methods raises the question whether they all yield the same results.

Recently, Rautu *et al.*[24] pointed out that in phase contrast imaging, projections of out-of-focus fluctuations may contribute to the contour statistics leading to systematic overestimation of the bending rigidity value when compared to other methods such as micropipette aspiration and X-ray scattering. However, comparing bending rigidity numbers obtained by different techniques is only meaningful if the same system is probed. It is known that many factors such as sugars (and gravity), salt, buffers, solution asymmetry, concentration of fluorescent lipids, preparation method or type of bilayer configuration (stacked or free-floating), influence the measured mechanical properties of bilayer membranes;[1,17,26–30] see Table S1 in the ESI† for a list of reported bending rigidity of DOPC membranes. For example, even measurements with the same method can give a wide range of values, *e.g.*, the bending rigidity of a DOPC bilayer measured with flickering spectroscopy has been reported from $15k_BT$[23] to $30k_BT$,[19] where k_BT is the thermal energy.

In order to compare imaging with phase contrast and confocal microscopy, which was suggested in Rautu *et al.*[24] as a better technique due to the precise control over the focal depth, we measure the bending rigidity of the same giant vesicle with both techniques. We highlight some important issues to be considered to ensure reliable measurements. We also show that results obtained with both methods are consistent.

Equilibrium fluctuations of a quasi-spherical vesicle

First, we summarize the theoretical basis of the fluctuations analysis (details are provided in ESI,† Section S6). We also correct published expressions for the relaxation frequency and cross-spectral density of the shape fluctuations.

The contour in the equatorial plane of a quasi-spherical vesicle is decomposed in Fourier modes, $r(\phi;t) = R_0\left(1+\sum_{q=-q_{\max}}^{q_{\max}} u_q(t)\exp(iq\phi)\right)$, where $R_0 = (3V/4\pi)^{1/3}$ is the radius of an equivalent sphere with the volume V of the GUV and q is the mode number. In practice, $q_{\max}$ is the maximum number of experimentally resolved modes. The statistical analysis of the fluctuating amplitudes u_q yields the values of

[a] Department of Mechanical Engineering, McCormick School of Engineering and Applied Science, Northwestern University, Evanston, Illinois 60208, USA. E-mail: Petia.Vlahovska@northwestern.edu
[b] Max Planck Institute of Colloids and Interfaces, Science Park Golm, 14424 Potsdam, Germany. E-mail: Rumiana.Dimova@mpikg.mpg.de
[c] Department of Engineering Sciences and Applied Mathematics, McCormick School of Engineering and Applied Science, Northwestern University, Evanston, Illinois 60208, USA

† Electronic supplementary information (ESI) available. See DOI: 10.1039/d0sm00943a

Open Access Article. Published on 17 September 2020. Downloaded on 10/1/2020 12:25:56 PM. This article is licensed under a Creative Commons Attribution 3.0 Unported Licence.

Open Access Article. Published on 17 September 2020. Downloaded on 10/1/2020 12:25:56 PM.
This article is licensed under a Creative Commons Attribution 3.0 Unported Licence.

membrane bending rigidity κ and the tension σ since $\langle|u_q|^2\rangle \sim k_BT/\kappa(q^3 + \boldsymbol{\sigma} q)$, where $\boldsymbol{\sigma} = \sigma R_0^2/\kappa$.

More precisely, the statistics of the two-dimensional circular modes, u_q, is derived from the three-dimensional shape modes, f_{lm}, which describe the nearly-spherical shape in terms of spherical harmonics,[13,31] $R(\theta;\phi;t) = R_0\left(1 + \sum_{l=0}^{l_{max}}\sum_{m=-l}^{l} f_{lm}(t)\,Y_{lm}(\theta;\phi)\right)$. Here, l_{max} is an upper cutoff, in the order of the ratio of the GUV radius and bilayer thickness. The contour in the focal plane corresponds to the equator of the quasi-spherical vesicle, $\theta = \pi/2$, *i.e.*, $r(\phi;t) = R\left(\frac{\pi}{2};\phi;t\right)$, which leads to the following expression for the mean squared amplitudes

$$\left\langle |u_q|^2 \right\rangle = \frac{k_BT}{\kappa}\sum_{l=q}^{l_{max}} n_{lq} P_{lq}^2(0)[(l-1)(l+2)(l(l+1)+\boldsymbol{\sigma})]^{-1} \quad (1)$$

where $n_{lq} = (2l + 1)(l - q)!/4\pi(l + q)!$ and P_{lq} are the associated Legendre polynomials. The short-wavelength shape fluctuations are dominated by the bending rigidity, while the long wavelengths are controlled by tension; the crossover occurs around mode $q_c = \sqrt{\boldsymbol{\sigma}}$.

To validate our methodology, we have simulated the thermal shape fluctuations of a GUV, see also ESI,† Section S6. We have generated a sequence of three-dimensional shapes (and their corresponding equatorial contours) using the evolution equations[31,32]

$$\frac{df_{lm}}{dt} = -\tau_l^{-1} f_{lm} + \zeta_{lm}(t);$$
$$\tau_l^{-1} = \frac{\kappa}{\eta_{ex} R_0^3}\frac{(l-1)l(l+1)(l+2)(l(l+1)+\boldsymbol{\sigma})}{4l^3 + 6l^2 - 1 + (2l^3 + 3l^2 - 5)\left(\frac{\eta_{in}}{\eta_{ex}} - 1\right)} \quad (2)$$

where ζ_{lm} is the thermal noise driving the membrane undulations, η_{in} and η_{ex} are the viscosity of the solution inside and outside the vesicle. Note that the relaxation time given by eqn (2) in Rautu *et al.*[24] has incorrect dependence on the viscosities of the enclosed and suspending solutions (this mistake is unlikely to affect the reported fluctuation spectra). The simulated contours were analyzed by our code and the extracted bending rigidity and tension were compared to the input values to confirm accuracy of the contour detection, Fourier decomposition and data fitting algorithms. The time evolution of the modes also enables us to access information provided by the time correlations $\langle u_q(0)u_q^*(t)\rangle = \langle|u_q|^2\rangle \exp(-t/\tau_q)$. If $q \gg 1$, the correlation time tends to that of a planar membrane $\tau_q^{-1} = \kappa(q^3 + \boldsymbol{\sigma} q)/2R_0^3(\eta_{ex} + \eta_{in})$. If the cross-spectral density $\langle|u_q(0)||u_q(t)|\rangle$ is utilized, the correct time dependence in the exponential includes a factor of 2 and eqn (3) in Zhou *et al.*[33] needs to be corrected (see ESI,† Section S6, eqn (39)).

Bending rigidity obtained from confocal and phase-contrast microcopy: effect of resolution and vesicle size

Giant unilamellar vesicles (GUV) were electroformed from DOPC (99.8 mol% dioleoylphosphatidylcholine and 0.2 mol% Texas-Red 1,2-hexadecanoyl-*sn-glycero*-3-phosphoethanolamine, TR-DHPE) in 20 mM sucrose and subsequently diluted in 22 mM glucose, see ESI,† Section S2 for details. Low sugar concentration was used in order to minimize the effects of gravity[28] and effect of sugars,[26] but still allow the vesicles to settle to the chamber bottom for easier recording. Low dye content minimizes effects of fluorophores.[29]

Fig. 1 shows a typical fluctuations spectrum, given by eqn (1), fitted to the experimental data for the same vesicle imaged with confocal and phase contrast microscopy using a 40× objective with 0.6 numerical aperture (NA), pinhole size of 1 Airy unit (AU) and polarization correction (see below and ESI,† Section S3). The contour was detected with sub-pixel resolution.[6] The experimental data was fitted with eqn (1) with Levenberg–Marquardt algorithm and yielded bending rigidity $\kappa = 23.9 \pm 1.6k_BT$ and tension $\sigma = 5.1 \pm 1.4 \times 10^{-9}$ N m^{-1} and $\kappa = 22.3 \pm 2.1k_BT$ and $\sigma = 3.1 \pm 1.2 \times 10^{-9}$ N m^{-1} from the confocal and phase contrast microscopy data, respectively. The average and error in individual GUV was determined by performing fluctuation spectroscopy 2–3 times. By imaging a population of 18 vesicles with both methods, the bending rigidity obtained are $22.5 \pm 2.0k_BT$ with confocal and $23.3 \pm 1.6k_BT$ phase contrast microscopy; each vesicle was analyzed with both imaging techniques as in Fig. 1 and then the results were averaged over the population. Fig. 2 shows the box and whisker plot for more detailed statistics. Based on F statistics and ANOVA (analysis of variance) test, the p-value obtained is $p = 0.48$ for null hypothesis testing. We also performed the paired-sample t-test and obtained $p = 0.43$. These p-values indicate no significant difference between the two imaging techniques.

Since only modes with wavenumber $q > \sqrt{\sigma R_0^2/\kappa}$ are sensitive to the bending rigidity, it is desirable to have more resolved

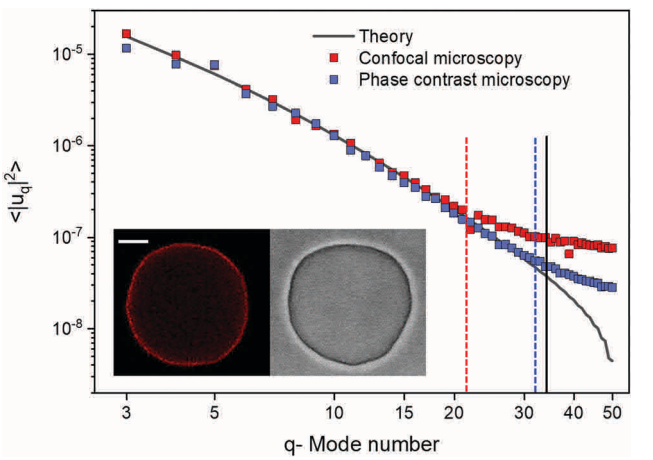

Fig. 1 Fluctuation spectrum of the same DOPC vesicle (shown in the inset) obtained with confocal and phase contrast microscopy with a 40×/NA 0.6 objective, pinhole size of 1 AU and polarization correction, see also ESI,† Movies S1 and S2. The dye concentration is 0.2 mol%. Scale bar is 15 μm. The vertical lines denote the cutoff resolution for the modes: optical resolution (solid line), phase contrast (blue dashed) and confocal (red dashed line). The theory is fitted to phase contrast data up to the mode marked by the dashed blue line. The crossover mode $q_c = \sqrt{\boldsymbol{\sigma}}$ is 7.

This journal is © The Royal Society of Chemistry 2020

Open Access Article. Published on 17 September 2020. Downloaded on 10/1/2020 12:25:56 PM.
This article is licensed under a Creative Commons Attribution 3.0 Unported Licence.

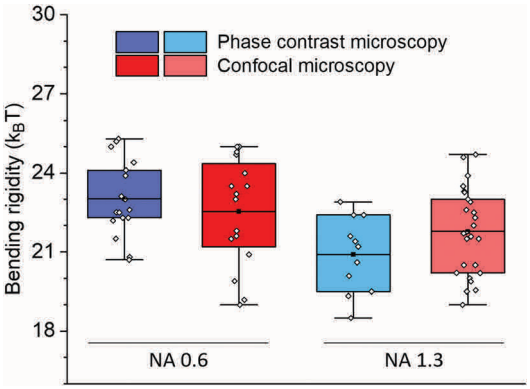

Fig. 2 Imaging with phase contrast and confocal microscopy for objectives of the same numerical aperture (NA) give consistent results. Box and whisker plot comparison for a DOPC vesicle population where each vesicle was analyzed with phase contrast and confocal imaging with 40× objectives with NA 0.6 and NA 1.3. Pinhole size is 1 AU with polarization correction. The dye concentration is 0.2 mol%.

modes, *i.e.*, modes with amplitude and wavelength greater than the optical resolution limit ≈250 nm.[34] The average mean fluctuation amplitude scales with the size of the vesicle $u_q \sim R_0\sqrt{k_BT/\kappa}$, hence larger GUVs admit more spatially resolvable fluctuation modes as shown in Fig. 3. However, even for the same vesicle we find that the number of resolved modes is higher for phase contrast than for confocal imaging. Indeed, Fig. 1 shows that the noise level is higher for confocal microscopy, and on average phase contrast imaging resolves 8–10 modes more than confocal imaging does. The poorer mode resolution with confocal microscopy is likely due to poor contour recognition. The reasons for this are discussed in the next section.

We found that the vesicle population needs to have broad range of radii to avoid a size bias in the bending rigidity values we discovered for confocal microscopy with low resolution optics, see also ESI,† Section S4. In the case of 40×/NA 0.6 (air) objective, the mean Pearson correlation and standard deviation coefficient is 0.65 ± 0.21 (see ESI,† Section S5 for the histograms generated with bootstrapping resampling technique). Analysis of a population of similar sized vesicles with radii around 10 μm underestimates κ by roughly $6k_BT$. The bias originates from out-of-plane fluorescence which worsens the contour detection. This issue is investigated in the next section and ESI,† Section S6. The size dependence is insignificant for phase contrast microscopy with a mean correlation coefficient of 0.28 ± 0.18 with 40×/NA 0.6 (air). Analyzing the same vesicle population with 40×/NA 1.3 objective in phase contrast and confocal imaging yields 21.0 ± $2.0k_BT$ and 21.7 ± $2.0k_BT$ respectively. Higher numerical aperture in phase contrast leads to negligible correlation coefficient of −0.07 ± 0.34 between bending rigidity and vesicle size and decrease in the correlation coefficient to 0.43 ± 0.14 for confocal imaging with 40×/NA 1.3 objective.

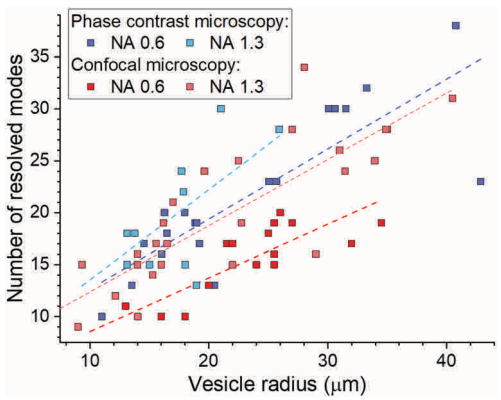

Fig. 3 Larger vesicles allow resolving more fluctuation modes thus yielding more reliable determination of the bending rigidity. Data are collected on DOPC vesicles with different sizes. The dye concentration is 0.2 mol%. Regression lines are added to guide the eyes. Imaging was done with 40× objectives with different numerical aperture (NA), pinhole size of 1 AU and polarization correction.

Out-of-focus fluorescence affects contour detection quality in confocal microscopy

The vesicle contour is detected from radial intensity line profiles, see ESI,† Section S2. In confocal cross sections, weak fluorescence from the vesicle membrane located above and below the focal plane may result in signal projected in the interior of the vesicle image which is higher compared to the surrounding background. The resulting asymmetry in the intensity line profile (Fig. 4a) leads to an artificial contour displacement, *i.e.*, poor contour detection (note that such an asymmetry is absent in images acquired with phase contrast microscopy of vesicles with similar refractive indices of the

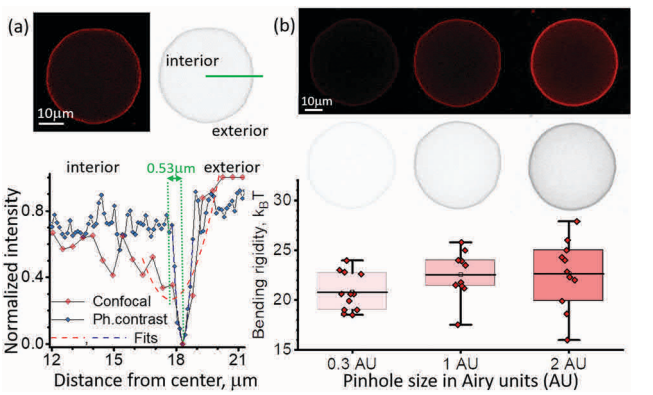

Fig. 4 Out-of-focus fluorescence in confocal images can result in erroneous contour detection and increased error in bending rigidity. (a) Intensity line profiles (gray-value) across the vesicle membrane (DOPC, with 0.2 mol% dye) are symmetric for phase-contrast images (blue) but asymmetric for confocal images (red, 1 AU). The asymmetry in the confocal line profile leads to incorrect detection of the contour position defined by the parabolic fit minimum, here, shifted inwards by 0.53 μm. (b) Vesicle images (and their inverted gray-value analogs) acquired with different pinhole size show increased fluorescence inside the vesicle which results in larger error in the bending rigidity. Box and whisker plot of the bending rigidity of the same DOPC vesicles imaged with confocal microscopy at three different pinhole sizes for 40×/NA 0.6 objective and polarization correction.

Open Access Article. Published on 17 September 2020. Downloaded on 10/1/2020 12:25:56 PM.
This article is licensed under a Creative Commons Attribution 3.0 Unported Licence.

internal and external solutions). This asymmetry creates a systematic error shifting the vesicle contour by 0.53 μm. The error is larger than the pixel resolution of the system, 0.252 μm, hence the higher modes are averaged out. Smaller vesicles or larger pinholes lead to higher signal inside the vesicle (see inset in Fig. 4b) corresponding to greater asymmetry which increases the error from contour fitting and introduces dependence of the bending rigidity on vesicle size. For imaging with higher numerical aperture objectives (*e.g.* NA 1.3), the asymmetry in the intensity line profiles is suppressed and contour detection is correct. Note that phase contrast images do not suffer from the asymmetry-induced error irrespective of the objective NA.

We investigated the impact of out-of-focus fluorescence on the fluctuations statistics by varying the pinhole size for confocal imaging on the same vesicle. The standard pinhole size in confocal microscopy is defaulted to 1 Airy unit (AU) (full width at half maximum FWHM = 1.6 μm) for 40×/NA 0.6 objective. We analyzed the same vesicles with different optical sectioning at 0.3 AU (FWHM = 0.9 μm), and 2 AU (FWHM = 2.9 μm). The mean bending rigidity did not show significant differences based on ANOVA testing, *post hoc* Dunnett test and paired-sample *t*-test (p = 0.87), however the error increases with the pinhole size. The sensitivity to the vesicle size also becomes more pronounced with higher pinhole size. At the largest pinhole size (2.0 AU) the Pearson correlation coefficient is 0.60 ± 0.22, while for 0.3 AU it becomes negligible, −0.14 ± 0.30.

Dye related artifacts: vesicle tubulation and polarization

Confocal imaging relies on fluorophores added to the membrane, and some studies have used up to 10 mol% dye.[22,23] To probe the effect of fluorophore on κ, we changed the dye concentration from 0.2 mol% to 2 mol% TR-DHPE. The bending rigidity of this population of vesicles showed non significant difference with $\kappa = 20.09 \pm 2.49 k_BT$ with one ANOVA testing. However, it was observed that over 2–3 min of recording, around 50% of the vesicles developed inward structures such as buds or visible tubes as shown in Fig. 5. Vesicles with such defects displayed significantly higher bending rigidity, $25.01 \pm 2.11 k_BT$.

TR-DHPE belongs to a family of polarity-sensitive fluorescent probes. As a result, the signal intensities are different at the pole and equator of the vesicle (see ESI,† Section S3). This may lead to errors in the contour detection in these regions. The polarization effect was corrected by using circular rotation plates to have even intensities across the equatorial vesicle plane. The analysis of the same vesicle with and without the polarization correction showed a $3k_BT$ lower bending rigidity without any correction with 40×/NA 0.6 (air) objective. This softening effect became insignificant with 40×/NA 1.3 (oil) objective (ESI,† Section S3). This is likely due to loss of signal at low intensity regions where the higher mode fluctuations intensities are averaged out with background noise due to out-of-focus fluorescence.

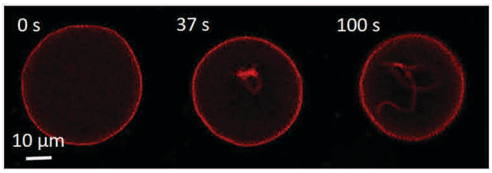

Fig. 5 Time lapse of a DOPC vesicle with 2 mol% TR-DHPE developing inward nanotubes as a result of long exposure to laser during confocal imaging. The second and third cross sections are non-equatorial to better show the formed nanotubes.

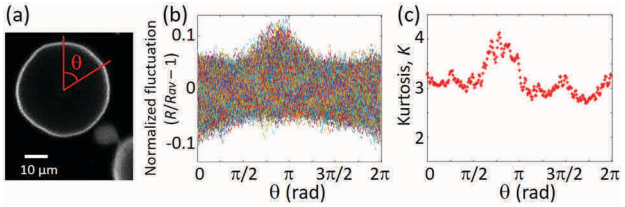

Fig. 6 Nearby structures affect the fluctuation spectrum. (a) A flickering vesicle in close proximity to another vesicle bud. (b) Fluctuation density map of the vesicle in (a): the fluctuations are modified by hydrodynamic interactions of the other flickering vesicle bud. (c) Kurtosis $K > 3$ indicates the vesicle fluctuations have amplified meaning local softening of the membrane.

Effect of nearby vesicles on fluctuation spectra

The equilibrium shape fluctuations of an isolated GUV are driven by Gaussian thermal noise. Defects such as buds, nanotubes, invaginations or docked LUVs modify the vesicle fluctuations[6] and their effect can be detected in the statistics at each point on the vesicle contour profile using the ensemble-averaged probability density function (PDF) as shown in Fig. 6a. In addition to defects attached the membrane, we also found that hydrodynamic flows and/or fluorescence signal from nearby vesicles can affect vesicle fluctuations.

We characterized the Gaussianity of the fluctuations using the fourth PDF moment, Kurtosis, K. For a Gaussian distribution, $K = 3$. In Fig. 6 we demonstrate how thermal fluctuations may be modified (see ESI,† Movie S3). As shown, the majority of contours are characterized by a normal distribution. However near other flickering structures, the fluctuation map density is modified. The non-Gaussian enhanced fluctuations are observed with leptokurtic nature ($K > 3$). This observation serves as a caution to filter out vesicles with sub-optical structures affecting the fluctuations.

Conclusions

We compare the bending rigidity of bilayer membranes determined from flickering spectroscopy of GUVs imaged with confocal and phase contrast microscopy. Examining the same

Open Access Article. Published on 17 September 2020. Downloaded on 10/1/2020 12:25:56 PM.
This article is licensed under a Creative Commons Attribution 3.0 Unported Licence.

vesicle with both imaging techniques shows no significant differences in the bending modulus obtained from the two methods, in contrast to the overestimation reported by Rautu *et al.*[24] when phase contrast microscopy is used. Our analysis indicates that membrane defects such as buds and tubes induced by long laser exposure in confocal microscopy can significantly stiffen the membrane. Furthermore, we find that errors in contour detection that could impact data interpretation can arise from fluorescence signal "pollution" and dye polarization. The bending rigidity we obtain ($\sim 22 k_B T$ for DOPC) is in line with the values obtained with other techniques such as micropipette aspiration, X-ray scattering, electrodeformation and neutron spin echo.[3,8,10] A scatter of approximately $2 k_B T$ is typical in the experiments and should be taken into account when comparing data from different groups and methods. Exploring the effect of various parameters, we find that optimal imaging conditions for bending rigidity measurements from confocal imaging include high magnification objective, high numerical aperture, circular polarization correction, minimum dye concentration, small pinhole size, and broad vesicle size distribution.

In conclusion, we demonstrate that phase contrast and confocal microscopy produce the same results if precautions are taken to minimize effects of the dye and improve contour detection. Our study suggests that the many published results obtained by phase contrast microscopy are likely to be unaffected by the projections of out-of-focus fluctuations onto the imaging plane in contrast to the claim by Rautu *et al.*[24] Since dye related artifacts such as laser-induced defects can compromise the data, it is advantageous to use phase contrast imaging as it does not require dyes.

Conflicts of interest

There are no conflicts to declare.

Acknowledgements

This research was funded in part by NSF-CMMI awards 1748049 and 1740011. PV acknowledges support from the Alexander von Humboldt Foundation and HAF acknowledges financial support from Prof. Reinhard Lipowsky for visits to the Max Planck Institute of Colloids and Interfaces. VNG and RD acknowledge support of the MaxSynBio consortium which is jointly funded by the Federal Ministry of Education and Research of Germany and the Max Planck Society. We thank Paul Salipante for proofreading the manuscript and M. Turner for useful suggestions. Open Access funding provided by the Max Planck Society.

Notes and references

1 R. Dimova, *Adv. Colloid Interface Sci.*, 2014, **208**, 225–234.
2 E. Evans and W. Rawicz, *Phys. Rev. Lett.*, 1990, **64**, 2094–2097.
3 W. Rawicz, K. Olbrich, T. McIntosh, D. Needham and E. Evans, *Biophys. J.*, 2000, **79**, 328–339.
4 M. Kummrow and W. Helfrich, *Phys. Rev. A: At., Mol., Opt. Phys.*, 1991, **44**, 8356–8360.
5 P. M. Vlahovska, R. S. Gracia, S. Aranda-Espinoza and R. Dimova, *Biophys. J.*, 2009, **96**, 4789–4803.
6 R. S. Gracia, N. Bezlyepkina, R. L. Knorr, R. Lipowsky and R. Dimova, *Soft Matter*, 2010, **6**, 1472–1482.
7 P. F. Salipante, R. Knorr, R. Dimova and P. M. Vlahovska, *Soft Matter*, 2012, **8**, 3810–3816.
8 A. Tian, B. R. Capraro, C. Esposito and T. Baumgart, *Biophys. J.*, 2009, **97**, 1636–1646.
9 B. Sorre, A. Callan-Jones, J.-B. Manneville, P. Nassoy, J.-F. Joanny, J. Prost, B. Goud and P. Bassereau, *Proc. Natl. Acad. Sci. U. S. A.*, 2009, **106**, 5622–5626.
10 N. Kučerka, Y. Liu, N. Chu, H. I. Petrache, S. Tristram-Nagle and J. F. Nagle, *Biophys. J.*, 2005, **88**, 2626–2637.
11 J. Pan, F. A. Heberle, S. Tristram-Nagle, M. Szymanski, M. Koepfinger, J. Katsaras and N. Kučerka, *Biochim. Biophys. Acta, Biomembr.*, 2012, **1818**, 2135–2148.
12 F. Brochard and J. F. Lennon, *J. Phys.*, 1975, **36**, 1035–1047.
13 J. Faucon, M. Mitov, P. Meleard, I. Bivas and P. Bothorel, *J. Phys.*, 1989, **50**, 2389–2414.
14 J. Pecreaux, H.-G. Dobereiner, J. Prost, J.-F. Joanny and P. Bassereau, *Eur. Phys. J. E: Soft Matter Biol. Phys.*, 2004, **13**, 277–290.
15 J. Genova, V. Vitkova and I. Bivas, *Phys. Rev. E: Stat., Nonlinear, Soft Matter Phys.*, 2013, **88**, 022707.
16 P. Bassereau, B. Sorre and A. Lévy, *Adv. Colloid Interface Sci.*, 2014, **208**, 47–57.
17 H. A. Faizi, S. L. Frey, J. Steinkühler, R. Dimova and P. M. Vlahovska, *Soft Matter*, 2019, **15**, 6006–6013.
18 H. Bouvrais, F. Cornelius, J. H. Ipsen and O. G. Mouritsen, *Proc. Natl. Acad. Sci. U. S. A.*, 2012, **109**, 18442–18446.
19 Y. Elani, S. Purushothaman, P. J. Booth, J. M. Seddon, N. J. Brooks, R. V. Law and O. Ces, *Chem. Commun.*, 2015, **51**, 6976–6979.
20 V. G. Almendro-Vedia, P. Natale, M. Mell, S. Bonneau, F. Monroy, F. Joubert and I. López-Montero, *Proc. Natl. Acad. Sci. U. S. A.*, 2017, **114**, 11291–11296.
21 P. Meleard, T. Pott, H. Bouvrais and J. H. Ipsen, *Eur. Phys. J. E: Soft Matter Biol. Phys.*, 2011, **34**, 116.
22 D. Drabik, M. Przybyłło, G. Chodaczek, A. Iglič and M. Langner, *Biochim. Biophys. Acta, Biomembr.*, 2016, **1858**, 244–252.
23 J. B. Dahl, V. Narsimhan, B. Gouveia, S. Kumar, E. S. G. Shaqfeh and S. J. Muller, *Soft Matter*, 2016, **12**, 3787–3796.
24 S. A. Rautu, D. Orsi, L. Di Michele, G. Rowlands, P. Cicuta and M. S. Turner, *Soft Matter*, 2017, **13**, 3480–3483.
25 A. F. Loftus, S. Noreng, V. L. Hsieh and R. Parthasarathy, *Langmuir*, 2013, **29**, 14588–14594.
26 V. Vitkova, J. Genova, M. D. Mitov and I. Bivas, *Mol. Cryst. Liq. Cryst.*, 2006, **449**, 95–106.
27 M. Karimi, J. Steinkühler, D. Roy, R. Dasgupta, R. Lipowsky and R. Dimova, *Nano Lett.*, 2018, **18**, 7816–7821.
28 J. R. Henriksen and J. H. Ipsen, *Eur. Phys. J. E: Soft Matter Biol. Phys.*, 2002, **9**, 365–374.
29 H. Bouvrais, T. Pott, L. A. Bagatolli, J. H. Ipsen and P. Méléard, *Biochim. Biophys. Acta, Biomembr.*, 2010, **1798**, 1333–1337.

30 H. Bouvrais, L. Duelund and J. H. Ipsen, *Langmuir*, 2014, **30**, 13–16.
31 U. Seifert, *Eur. Phys. J. B*, 1999, **8**, 405–415.
32 L. Miao, M. A. Lomholt and J. Kleis, *Eur. Phys. J. E: Soft Matter Biol. Phys.*, 2002, **9**, 143–160.
33 H. Zhou, B. B. Gabilondo, W. Losert and W. van de Wate, *Phys. Rev. E: Stat., Nonlinear, Soft Matter Phys.*, 2011, **83**, 011905.
34 R. Lipowsky, in *Structure and Dynamics of Membranes*, ed. R. Lipowsky and E. Sackmann, Handbook of Biological Physics, North-Holland, 1995, vol. 1, pp. 521–602.

Open Access Article. Published on 17 September 2020. Downloaded on 10/1/2020 12:25:56 PM.
This article is licensed under a Creative Commons Attribution 3.0 Unported Licence.

Supplemental materials: Fluctuation spectroscopy of giant unilamellar vesicles using confocal and phase contrast microscopy

Hammad A. Faizi,[ab] Cody J. Reeves,[c], Vasil N. Georgiev[b], Petia M. Vlahovska,[ac] and Rumiana Dimova*[b]
[a] *Department of Mechanical Engineering, Northwestern University, Evanston, IL 60208, USA*
[b] *Department of Theory and Biosystems, Max Planck Institute of Colloids and Interfaces, Science Park Golm, 14424 Potsdam, Germany.*
[c] *Department of Engineering Sciences and Applied Mathematics, Northwestern University, Evanston, IL 60208, USA.*
∗ *E-mails for correspondence Rumiana.Dimova@mpikg.mpg.de, Petia.Vlahovska@northwestern.edu*
(Dated: September 21, 2020)

S1. Bending rigidity value of DOPC bilayers

The bending rigidity values of bilayer membranes made of the same lipid can vary across studies due to different conditions, e.g., sugars, salt, buffers, dye concentration, as well as the preparation method [1]. Table I illustrates the wide range of reported values of the bending rigidity values DOPC bilayers. Refer to Table II for the bending rigidity values obtained in this study for different microscopy setting.

TABLE I: Different bending rigidity values for DOPC under different conditions and methods.PC, C and EP refer to phase contrast, confocal and epi-flourescent microscopies used respectively in Fluctuation spectroscopy.

Method	Rigidity (k_BT)	Dye conc. (%*mol*)	Buffer, Sugar (inside/outside)	Salt	Preparation
Fluctuation Spec. [EP,C]	14.9±0.4 [2]	15.8 NBD PC	100 mM Sucrose/100 mM Sucrose	N/A	Electroformation
Fluctuation Spec. [PC]	26.4±2.4 [3]	0 or 0.1 diIC18	10 mM Sucrose/10 mM Glucose	0.1 mM NaCl	Electroformation
Fluctuation Spec. [PC]	26.8±2.4 [4]	1.0 Liss Rhod PE	450 mM Sucrose/500 mM Glucose	N/A	Electroformation
Fluctuation Spec. [PC]	29.8±2.4 [4]	1.0 Liss Rhod PE	450 mM Sucrose/500 mM Glucose	N/A	Phase Transfer
Fluctuation Spec. [EP]	22.3±0.5 [5]	0.12 Liss Rhod PE	100 mM Sucrose/200 mM Sucrose	N/A	Electroformation
Fluctuation Spec. [PC]	27.3±3.2 [6]	N/A	100 mM Sucrose/100 mM Sucrose	2 mM NaN_3	Electroformation
Fluctuation Spec. [PC]	22.7±2 [7]	N/A	100 mM Sucrose/125 mM Glucose	N/A	Electroformation
Fluctuation Spec. [PC]	21.46±4 [8]	N/A	100 mM Sucrose/125 mM Glucose	N/A	Electroformation
Fluctuation Spec. [PC]	19±1 [9]	N/A	10 mM Sucrose/10 mM Glucose	N/A	Electroformation
Fluctuation Spec. [C]	19±1 [10]	0.8 TR DHPE	197 mM Sucrose/200 mM Glucose	N/A	Electroformation
Time Correlations	22.1 [11]	N/A	300 mM Sucrose/307 mM Glucose	N/A	Electroformation
Micropipette Aspiration	20.7±2 [12]	N/A	100 mM Sucrose/100 mM Glucose	N/A	Thin Film Hyd.
Micropipette Aspiration	22.8±2.2 [9]	N/A	8 mM Sucrose/8 mM Glucose	N/A	Electroformation
X- Ray Scattering	20±2 [13]	N/A	Water/Water	N/A	Extrusion
X- Ray Scattering	20.2±1.4 [14]	N/A	Deionized water	N/A	Bilayer stack
Electrodeformation	21.9±2 [3]	0.1 diIC18	10 mM Sucrose/10 mM Glucose	0.1 mM NaCl	Electroformation
Tether pulling	20±2 [15]	0.3 TR DHPE	300 mM Sucrose/80 mM Glucose	100 mM NaCl	Electroformation
Neutron Spin Echo	20±1 [16]	N/A	D_2O/D_2O	0 mM	Extrusion
Neutron Spin Echo	20±2 [17]	N/A	D_2O/D_2O	0 mM	Extrusion
Neutron Spin Echo	30±4 [17]	N/A	D_2O/D_2O	150 mM	Extrusion
Neutron Spin Echo	40±5 [17]	N/A	D_2O/D_2O	470 mM	Extrusion
Interferometry	10.5±8.8 [18]	N/A	295 mM Sucrose/300 mM Glucose	N/A	Electroformation

TABLE II: Bending rigidity values obtained in this study for DOPC under different conditions and microscopy settings. Note the sugar concentration is the same in all the experiments: 20 mM Sucrose inside/ 22 mM Glucose outside. The dye used is TR DHPE and all the vesicles were formed via electroformation.

Microscopy	Rigidity (k_BT)	Dye conc. ($\%mol$)	Objective/NA	Polarization Correction	Pinhole (A.U)
Phase Contrast	19.4±2.1	0.2	100x/1.25	N/A	N/A
Phase Contrast	22.5±1.5	0	40x/0.6	N/A	N/A
Phase Contrast	23.3±1.6	0.2	40x/0.6	N/A	N/A
Phase Contrast	21.0±2.0	0.2	40x/1.3	N/A	N/A
Confocal	21.7±2.0	0.2	40x/1.3	Yes	1
Confocal	22.5±2.1	0.2	40x/0.6	Yes	1
Confocal	22.5±2.4	0.2	40x/0.6	Yes	0.3
Confocal	22.6±3.5	0.2	40x/0.6	Yes	2
Confocal	20.4±4.0	0.2	40x/0.6	No	1
Confocal	22.3±1.6	0.2	40x/1.3	No	1
Confocal	25.0±2.1	2.0	40x/0.6	Yes	1

S2. Methods

Vesicle preparation

Giant unilamellar vesicles (GUVs) were prepared using the classical electroformation method [19] from DOPC and the fluorescent lipid Texas Red 1,2-hexadecanoyl-sn-glycero-3-phosphoethanolamine (TR-DHPE). The composition of the GUVs explored are 99.8 % DOPC 0.2 % TR-DHPE and 98 % DOPC 2 % TR-DHPE (mole fractions). Stock solutions of DOPC and TR-DHPE at 10 mg/ml and 1 mg/ml in chloroform were diluted to a final concentration of 4 mM for varying proportions. A small volume, 10 μl, of the solution was spread on the conductive surface of two glass slides coated with indium tin oxide (ITO) (Delta Technologies). The glass slides were then stored under a vacuum for 1–2 hours to remove traces of organic solvent. Afterwards, a 2 mm Teflon spacer was sandwiched between the glass slides and the chamber was gently filled with 20 mM sucrose solution. The slides (conductive side facing inward) were connected to an AC signal generator Agilent 33220A (Agilent Technology GmbH, Germany). An AC field of voltage 1.5 V and frequency 10 Hz applied for 2 hours at room temperature, resulting in 10-50 μm sized vesicles. The harvested vesicles were diluted 10 times in 22 mM glucose solution to obtain fluctuating vesicles. All GUVs were analyzed within 8 hours of electoformation.

Microscopy and video recording

The equatorial fluctuations for both phase contrast and confocal mode were recorded with Leica TCS SP8 scanning confocal microscope using a HCX PL APO 40x/ Numerical Aperture (NA) 0.6 Ph2 (air) objective and a HC PL APO 40x/ NA 1.3 (oil) objective. The pinhole size during the experiment was fixed to 1 AU (Airy units) unless stated otherwise. Table 1 compiles the pixel size and focal depth for different experimental conditions. The scanning speed was fixed to 1 kHz in bidirectional mode and the polarizer plates were rotated (100%) to remove the polarization effect of the fluorescent dye unless stated otherwise. The dye was excited with a 561 nm laser (diode-pumped solid-state laser) with 1.61% (laser intensity) HyD3 detector (hybrid) and the gain was fixed to 23%. Phase contrast imaging was recorded with PCO CS dimax (PCO AG, Kelheim, Germany)) mounted on confocal microscope. 1500-2000 images were recorded at 3.83 frames per second (fps) with confocal and 60 fps with phase contrast imaging. The RGB confocal images were converted to 8 bit and then inverted. We implemented an inbuilt MATLAB sobel disk filter $fspecial('sobel')$ and image normalization to increase the contrast of the contour.

In this section, we list different focal depths and pixel sizes for different microscopy and numerical aperture settings for 40x objective. Focal depth or FWHM (full width half maximum) of phase contrast imaging was determined using the standard formula $d = \frac{\lambda}{NA^2}$ The wavelength of transmission light was assumed to be 550 nm.

TABLE III: Different experimental conditions for video recording with 40x objective.

Microscopy	Numerical Aperture	Medium	Pinhole size (AU)	Focal depth (μm)	Pixel Resolution (nm)
Phase contrast	0.6	Air	1	1.57	276.9
Phase contrast	1.3	Oil	1	0.35	158.7
Confocal	0.6	Air	1	1.61	252.7
Confocal	1.3	Oil	1	0.52	252.7

TABLE IV: Focal depth or FWHM (full width half maximum) for confocal imaging.

Medium	Pinhole size (AU)	Focal depth (μm)
Air	0.3	0.9
Air	1	1.6
Air	2	2.9

Sub-pixel contour recognition

The intensity profile in the radial direction for N wedges were determined from three different interpolation schemes (Gaussian, parabolic and linear weighting of neighbouring pixel) for sub-pixel contour recognition. This was done to check if different interpolation schemes affects the bending rigidity values due to uncertainty introduced at higher wave-numbers for experimental vesicle contour fluctuations. The mean bending rigidity obtained was similar for all the three schemes for the same vesicle. Figure (S1) illustrates the subpixel accuracy determination for a 35 μm radius vesicle. The bending rigidities obtained was 22.0$\pm$3.0 $\mathrm{k}_B T$, 21.1$\pm$1.0 $\mathrm{k}_B T$ and 21.9$\pm$2.2 $\mathrm{k}_B T$ from Gaussian, parabolic and linear interpolation schemes respectively.

S3. Polarization Effects

We analyzed the same vesicle with and without polarization effects. The polarization effects were corrected using circular plates that were rotated 100%. Figure (S2) illustrates the effect of dye polarization for vesicles imaged with different numerical apertures. Using one Anova test, we find a significant difference of 3 $\mathrm{k}_B T$ for the 40x/0.6 NA case. The difference tends to be negligible for 40x/1.3 NA case.

S4. Effect of Vesicle Size on Bending Rigidity Values

The bending rigidity obtained from confocal microscopy with low-resolution optics (e.g. 40x objective, NA 0.6, 1 AU, polarization correction) can be systematically underestimated if the vesicle population contains similar sized vesicles. We demonstrate this by comparing the bending rigidity of the same vesicle imaged with confocal and phase-contrast microscopy, see Figure (S3). Vesicles with smaller sizes yield apparently lower bending rigidity, see Fig. S4 which further highlights the bias effect. For small vesicles, the out-of-focus signal gives rise to asymmetry in the contour intensity (illustrated in Fig. 4a in the main text) which leads to errors in the contour detection and underestimation of the bending rigidity. When the refractive index difference across the membrane is small (as is the case in our experiments), phase contrast imaging does not suffer from this size bias.

S5. Bootstrapping resampling

Details about the various statistical techniques can be found in Ref. [20]. Here we explain the bootstrapping sampling technique. A more rigorous reference is the textbook [21]. In practice, the finite amount of data or length of experiment limits the accuracy to infer data confidently. Bootstrapping is an inference method about the population from a given sample. In bootstrap-resamples, the population is in fact the sample and this quantity is known. This allows to measure the quality of inference of the 'true' sample from a re-sampled data. For example, let's consider the average mass of the human population world wide. It is difficult to measure the mass of every individual globally, therefore, a small sample is measured. Let's assume the sample size of N people. From that sample size, only one mean can be measured. In order to have a reasonable estimate about the population statistics, we need to have variability

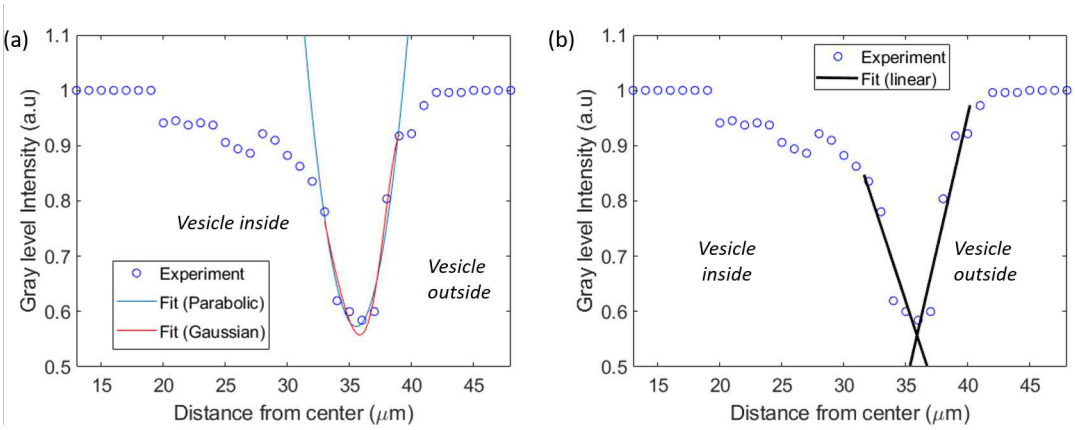

Fig. S 1: Intensity profile for a vesicle contour obtained from confocal imaging. The contour recognition details are given in [3]. The sub-pixel accuracy of the contour profile is determined based on (a) Gaussian, parabolic and (b) linear interpolations

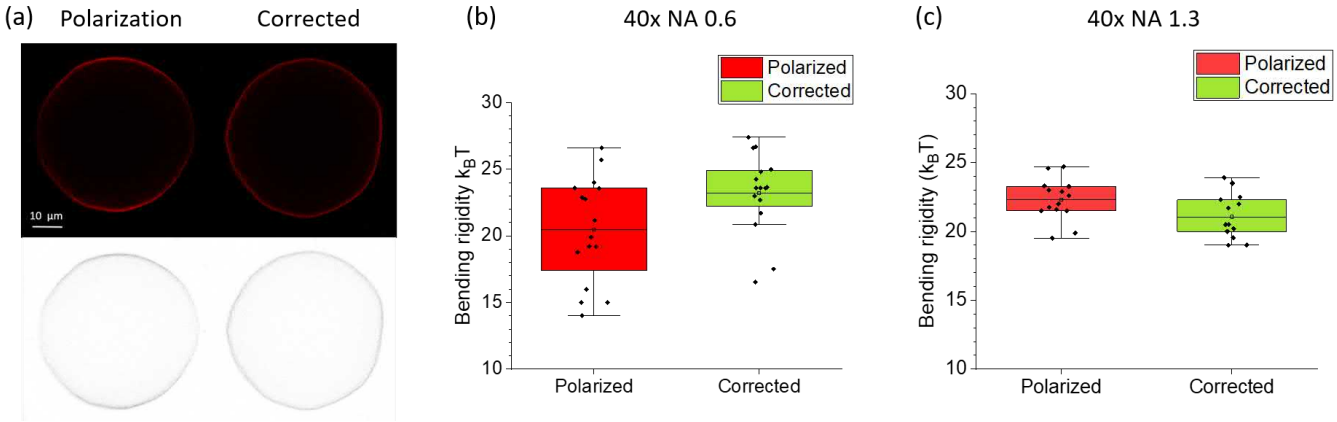

Fig. S 2: Polarization effects. (a) Confocal images of the same vesicle with and without polarization effects for 40x/0.6 NA case. The polarization effects were removed using circular plates that were rotated 100%. (b, c) Comparison between the same vesicles for different numerical apertures. Using one Anova test, we find a significant difference of 3 k_BT for 40x/0.6 NA case. The difference tends to be negligible for 40x/1.3 NA case. Pinhole size is 1 AU.

of the mean that we computed. The simplest bootsampling statistics can be considered by taking the original data N individuals and resampling to create a new sample of the same size N (e.g. we might 'resample' 10 times from [60,61,62,63,64,65,66,67] kg and get [61,64,63,63,60,60,62,65] kg). This process is repeated a large number of times, 100 to 10000, to create a histogram that be applied to any estimator testing. Bootstrap resampling was carried out using MATLAB's *bootstrp ()*.

In the case of our experiments, the finite amount of data or length of experiment limits the accuracy to infer data confidently. The bootstrap resampling requires choosing random replacement from a given data set and examining each sample the same way. This way a particular data point from the original set can reappear randomly multiple times in a particular bootstrap sample. The element size of the bootstrap sample is the same as the element size of the original data. This technique allows to obtain uncertainty of the quantity one estimates.

Bootstrap resampling algorithm for estimating standard error [21]:
1. Obtain N independent bootstrap samples $X^{*1}, X^{*2}, X^{*3}, ...X^{*N}$, each consisting of n data values drawn with a replacement from x where $x = [x^1, x^2, x^3...x^n]$. Note for estimating a standard error, the number N will ordinarily be larger than 30 to satisfy the Central Limit Theorem. Computations allow to use a large number N such as 10^3 to 10^4.
2. Determine the bootstrap replication for every bootstrap resample:

$$\zeta^*(b) = s(X^{*b}) \qquad b = [1, 2, 3, ..N] \tag{1}$$

where $s()$ is a statistical function like sample mean. For example, if $s(x)$ is the sample mean $\bar{x}$ then $S(X^*)$ is the

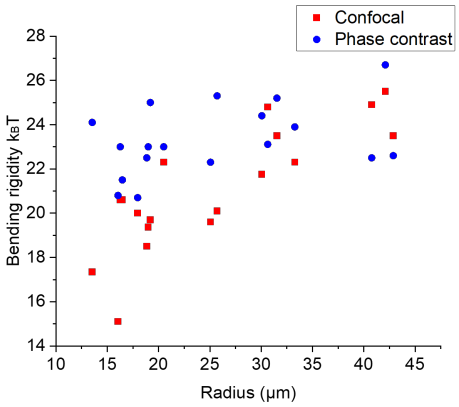

Fig. S 3: Vesicle size effects. Every vesicle was imaged with confocal and phase contrast microscopy. Data are collected on DOPC vesicles with different sizes. The dye concentration was 0.2 mol. Imaging was done with 40x objectives with NA 0.6, 1 AU and polarization correction.

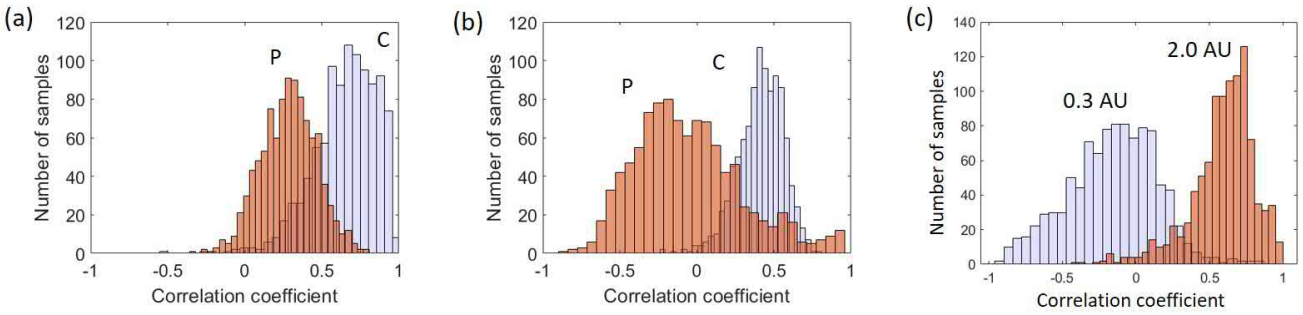

Fig. S 4: Bootstrap method with 95% confidence to evaluate bending rigidity dependence on size of vesicles for different numerical aperture (a) 40x/0.6 NA, (b) 40x/1.3 NA in phase contrast (P) or confocal(C) microcopy, and the pinhole sizes (c) (blue AU 0.3 and red AU 2).

mean of bootstrap data set.
3. Compute the standard error SE by utilizing the standard deviation of N replications

$$SE = \left[\frac{\sum_{b=1}^{N}[\zeta^*(b) - \zeta^*(.)]}{N-1}\right]^{\frac{1}{2}} \tag{2}$$

where $\zeta^*(.) = \sum_{b=1}^{N} \zeta^*(b)/N$.

In our case we determine the SE of mean Pearson correlation using bootsampling statistics.

S6. Numerical simulations of vesicle contours

Mathematical Model

The total energy of the system is given by the Helfrich model[22] as Eq. (3) where κ is the bending rigidity, c_1 and c_2 are the local radii curvatures, A is the total surface area, V is the interior volume of the vesicle, σ is the surface tension, and p is the pressure difference across the membrane.

$$F = \frac{\kappa}{2}\int_A (c_1 + c_2)^2 dA + \sigma A + pV \tag{3}$$

For a quasi-spherical vesicle in equilibrium, the shape can be decomposed into spherical harmonics ($\mathcal{Y}_{lm}$) such that the position of the surface is given by

$$R(\theta,\phi,t) = R_0\left(1+\sum_{l=0}^{l_{max}}\sum_{m=-l}^{l} f_{lm}(t)\mathcal{Y}_{lm}(\theta,\phi)\right) \tag{4}$$

where the characteristic radius R_0 is given by $V=\frac{4}{3}\pi R_0^3$. The spherical harmonics are defined as

$$\mathcal{Y}_{lm} = n_{lm}P_{lm}(\cos\theta)e^{\mathrm{i}m\phi}, \quad n_{lm}=\sqrt{\frac{(2l+1)(l-m)!}{4\pi(l+m)!}} \tag{5}$$

$P_{lm}(\cos\theta)$ are the associated Legendre polynomials.

As $l=1$ account for translational modes, for the sake of this paper, $f_{lm}(t)$ will be restricted to $f_{1m}(t)=0$ for $l=1$. Furthermore, volume conservation requires that [23]

$$f_{00} = \frac{-1}{\sqrt{4\pi}}\sum_{l=2}^{l_{max}}\sum_{m=-l}^{l}|f_{lm}|^2. \tag{6}$$

Assuming there is no external fluid flow, the harmonic coefficients (f_{lm}) for $l>1$ are described by the following

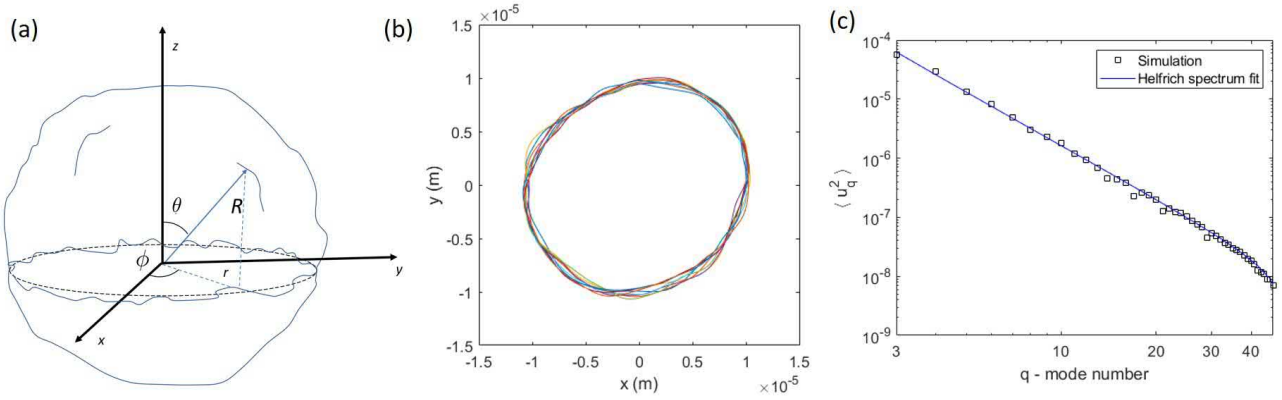

Fig. S 5: (a) A sketch of a GUV. (b) Time sequence of vesicle contours taken at time intervals of 1 s; the bending rigidity is $\kappa = 1\times10^{-19}$ J and the membrane tension is $\sigma = 1\times10^{-9}$ N/m. The size of the vesicle is $R_0 = 10^{-5}$ m. (c) Helfrich mode spectrum determined by the image detecting algorithm based on Ref. [3]. The spectrum was fitted with Equation 2 from the main text to obtain the bending rigidity and membrane tension.

stochastic differential equation [23]

$$\partial_t f_{lm} = -\tau_l^{-1} f_{lm} + \zeta_{lm}(t) \tag{7}$$

where

$$\tau_l = \frac{\eta_{\mathrm{ex}}R_0^3}{\kappa\Gamma_l(\lambda)E_l}, \quad \Gamma_l = \frac{l(l+1)}{4l^3+6l^2-1+(2l^3+3l^2-5)(\lambda-1)} \quad \text{and} \quad E_l=(l+2)(l-1)\Big(l(l+1)+\bar{\sigma}\Big). \tag{8}$$

A tutorial derivation of the evolution equation and the relaxation time (in the absence of thermal noise) can be found in Refs. [24, 25] The dimensionless tension is $\bar{\sigma}=\sigma R_0^2/\kappa$. $\lambda=\eta_{\mathrm{in}}/\eta_{\mathrm{ex}}$ is the ratio of viscosities of the solutions inside and outside the vesicle. When $\lambda=1$, our result for the relaxation time reduces to the one reported by Refs. [23, 26]. To make easier comparison with the result of Ref. [10], we can rewrite the relaxation time as

$$\tau_l = \frac{R_0^3}{\kappa}\frac{\eta_{\mathrm{ex}}\left(2l^3+3l^2+4\right)+\eta_{\mathrm{in}}\left(2l^3+3l^2-5\right)}{l(l+1)(l+2)(l-1)\Big(l(l+1)+\bar{\sigma}\Big)} \tag{9}$$

$\zeta_{lm}(t)$ is a stochastic term accounting for thermal noise; the corresponding time correlation is given as

$$\Big\langle\zeta_{lm}(t)\zeta_{l'm'}(t')\Big\rangle = (-1)^m\,\frac{2k_BT\Gamma_l}{\eta_{\mathrm{ex}}R_0^3}\,\delta_{l,l'}\delta_{m,-m'}\delta(t-t'). \tag{10}$$

The δ functions are the traditional Kronecker and Dirac delta functions. From Eq. 10, the variance of $\zeta_{lm}(t)$ is given by

$$\left\langle |\zeta_{lm}|^2 \right\rangle = 2\frac{k_B T \Gamma_l}{\eta_{\rm ex} R_0^3} = 2\Sigma_l. \tag{11}$$

Numerical Method

At this point, it is convenient to decompose f_{lm} and ζ_{lm} into real and imaginary components such that $f_{lm}(t) = X_{lm}(t) + \mathrm{i}\, Y_{lm}(t)$ and $\zeta_{lm}(t) = a_{lm}(t) + \mathrm{i}\, b_{lm}(t)$. As a_{lm} and b_{lm} are independent of each other then

$$\left\langle |\zeta_{lm}|^2 \right\rangle = \left\langle |a_{lm}|^2 \right\rangle + \left\langle |b_{lm}|^2 \right\rangle = 2\left\langle |a_{lm}|^2 \right\rangle = 2\left\langle |b_{lm}|^2 \right\rangle = 2\Sigma_l \tag{12}$$

Eq. (7) can then be rewritten as

$$\partial_t X_{lm} = -\tau_l^{-1} X_{lm} + a_{lm}(t) \tag{13}$$

and similarly for Y_{lm}. As Eq. (13) is a simple Langevin equation, the exact time update [27] is given as

$$X_{lm}(t+\Delta t) = X_{lm}(t) e^{-\Delta t/\tau_l} + \left[\frac{1}{2}\Sigma_l^2 \tau_l \left(1 - e^{-2\Delta t/\tau_l}\right)\right]^{1/2} n \tag{14}$$

such that Δt is the time step size and n is a sample value from the normal distribution $\mathcal{N}(0,1)$. In order to properly resolve the dynamics of the higher order coefficient, a sufficiently small time step must be chosen so that $\Delta t << \tau_{l_{\max}}$. Yet as each harmonic coefficient is independent of each other, Eq. 14 can be evaluated for all X_{lm} and Y_{lm} simultaneously. Given all the harmonic coefficients (f_{lm}), the cross-section at the equator, $R(\theta = \pi/2)$, can easily be computed using Eq. (4).

When running the numerical simulations, the user has some choice of which input parameters to specify. For example, one can specify the effective surface tension (dimensionless) $\bar{\sigma}$ and the largest incorporated mode l_{max}. In this case, the vesicle's excess is obtained from [23]

$$\alpha = \frac{\mathrm{k}_B T}{2\kappa}\left[\frac{5}{6+\sigma} + \ln\left(\frac{l_{max}^2 + \bar{\sigma}}{12 + \bar{\sigma}}\right)\right], \tag{15}$$

Alternatively, one can specify α and $\bar{\sigma}$, and Eq.(15) then provides the requisite l_{max}.

Here we demonstrate an example of a numerically simulated vesicle with predefined bending rigidity and membrane tension. Figure (S5)b shows a time sequence of equatorial vesicle contours with bending rigidity of $\kappa = 10^{-19}$ J and membrane tension of $\sigma = 10^{-9}$ N/m. The size of the vesicle is $R_0 = 10^{-5}$ m. By implementing our image detection technique and fitting algorithm from *Gracia et al.*[3], we are able to reproduce the bending rigidity and membrane tension respectively as $\kappa = (1.00 \pm 0.01) \times 10^{-19}$ J and $\sigma = (1.1 \pm 0.2) \times 10^{-9}$ N/m with the Helfrich spectrum given in Figure (S5). Notably our image detection is able to resolve more than 45 shape fluctuation modes.

Simulating the Effect of Out-of-focus Signal

Due to a finite focal depth, the microscope imaging does not capture only the optical/fluorescence signal at the focal (equatorial) plane. The out-of-focus signal results in gradient in the image intensity near the focal plane vesicle contour.

To simulate this effect, we numerically projected the vesicle shape $R(\theta, \phi, t)$ on the equatorial plane and assigned intensity of the projected location, $R(\theta, \phi, t)\sin\theta$, given by

$$I(r, \phi, t) = \int_0^{2\pi} \int_{\frac{\pi}{2}-\theta_{fd}}^{\frac{\pi}{2}+\theta_{fd}} W(\theta')\ \delta(\phi - \phi')\ \delta(r - R(\theta', \phi', t)\sin\theta')\ d\theta' d\phi', \tag{16}$$

where $\frac{\pi}{2} \pm \theta_{fd}$ are the top and bottom of the microscope focal depth (FD), $\theta_{fd} = \arctan(FD/R_0)$. $W(\theta)$ is the intensity weighting function

$$W(\theta) = \frac{1}{W_0} \exp\left[-\frac{\cos^2(\theta)}{2\cos^2(\theta_{fd})}\right] \tag{17}$$

and W_0 is the corresponding normalization constant. The resulting images of the equatorial plane at different focal depth are illustrated in Figure S6a.

We varied the magnitude of the focal depth FD, from 0 to $0.3R_0$. The fluctuation spectra obtained for the simulations are shown in Figure S6b for a vesicle sized $R_0 = 20\,\mu m$ with κ= 22 k_BT and $\sigma = 1.4\times10^{-9}$ N/m. The crossover mode $q_c = \sqrt{\bar{\sigma}} \sim 3$. The effect of the projections is only significant for modes $q \geq \Delta^{-1}$, where $\Delta = \frac{FD}{R_0}$ [10]. For smaller values of $\Delta < 0.05$, the projections have no effect - the spectra overlap implying same bending rigidity. However, as the value of Δ increases, more modes get affected by the projections resulting in an effective softening of the membrane from 22 k_BT to 19 k_BT, see S6c.

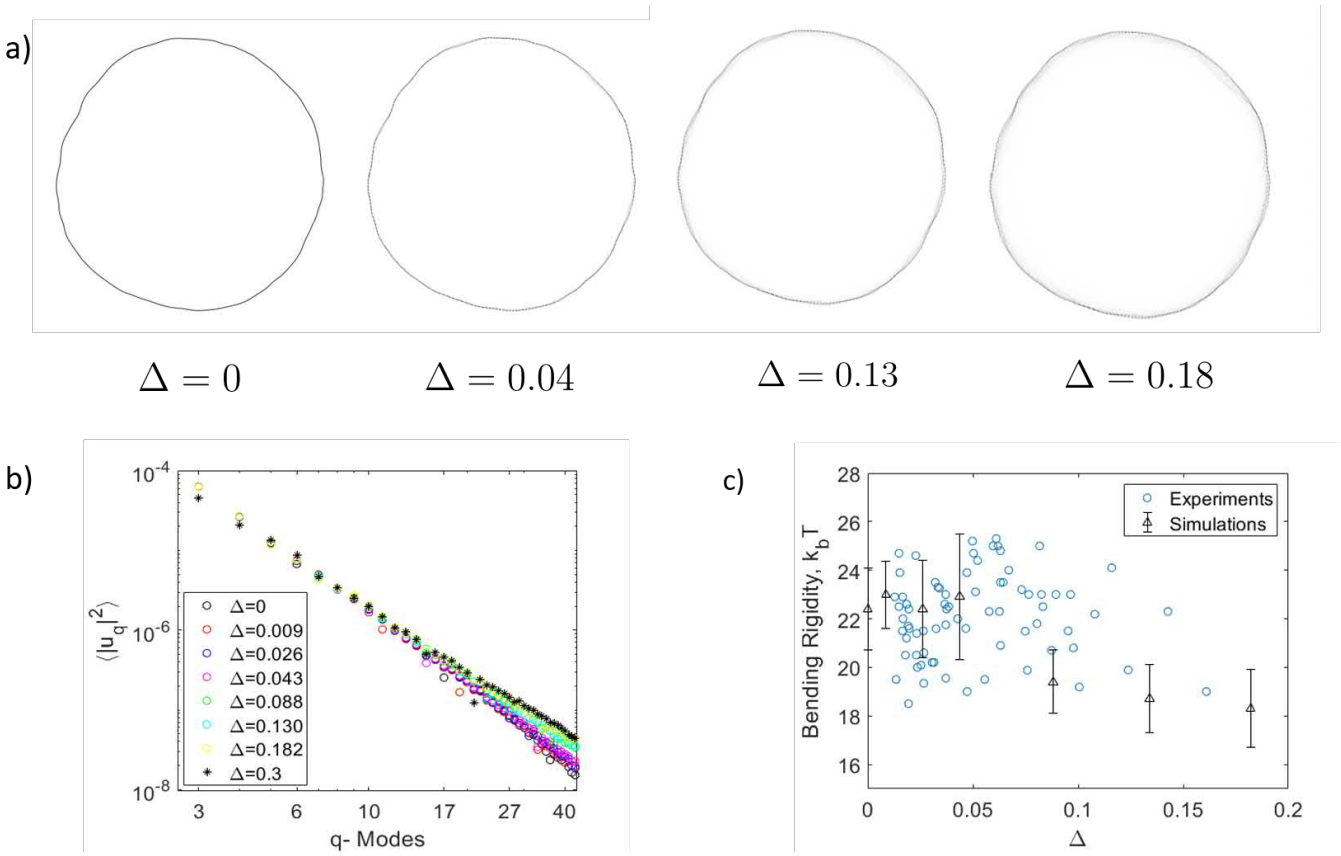

Fig. S 6: a) Snapshot of vesicle equatorial contours at different $\Delta = FD/R_0$. The simulated vesicle has bending rigidity= 22 k_BT, membrane tension= 1.4×10^{-9} N/m and radius $R_0 = 20\,\mu m$. Each image was acquired over 0.2 s (corresponding to imaging rate of 5 fps). b) Fluctuation spectrum obtained at different Δ from the numerical simulations c) Bending rigidity obtained for different Δ. Here we have compared the experimental results with numerical simulations.

Fluctuations statistics: derivations of the basic results

Here we summarize the main results for the dynamics of a quasi-spherical vesicle.

Mean Squared Magnitude of the Fourier Modes: The dynamics of the spherical harmonics modes is governed by the following Langevin equation,

$$\frac{\partial f_{lm}}{\partial t} = -\tau_l^{-1}\ f_{lm} + \zeta_{lm} \tag{18}$$

where the relaxation time τ_l is given by Eq.(9) and the noise is

$$\left\langle \zeta_{lm} \right\rangle = 0 \text{ and } \left\langle \zeta^*_{lm}(t)\zeta_{l'm'}(t') \right\rangle = \frac{2\mathrm{k}_B T \Gamma_l}{\eta_{\mathrm{ex}} R_0^3}\delta(t-t')\delta_{ll'}\delta_{mm'}. \tag{19}$$

The analytic solution to Eq. (18) is given by

$$f_{lm}(t) = e^{-t/\tau_l} f_{lm}(0) + \int_0^t e^{-(t-t')/\tau_l} \zeta_{lm}(t') dt'. \tag{20}$$

and therefore

$$|f_{lm}(t)|^2 = e^{-2t/\tau_l}|f_{lm}(0)|^2 + \int_0^t e^{-(2t-t')/\tau_l}\Big(f_{lm}(0)\zeta^*_{lm}(t') + f_{lm}(0)^*\zeta_{lm}(t')\Big)dt' + \int_0^t\int_0^t e^{-(2t-t'-t'')/\tau_l}\zeta_{lm}(t')\zeta^*_{lm}(t'')dt'dt''. \tag{21}$$

The ensemble average of $\Big\langle |f_{lm}|^2 \Big\rangle$ of Eq. (21) is then

$$\Big\langle |f_{lm}|^2 \Big\rangle = e^{-2t/\tau_l}|f_{lm}(0)|^2 + \int_0^t e^{-(2t-t')/\tau_l}\left(f_{lm}(0)\Big\langle \zeta^*_{lm}(t')\Big\rangle + f_{lm}(0)^*\Big\langle \zeta_{lm}(t')\Big\rangle\right)dt' + \int_0^t\int_0^t e^{-(2t-t'-t'')/\tau_l}\Big\langle \zeta_{lm}(t')\zeta^*_{lm}(t'')\Big\rangle dt'dt''. \tag{22}$$

Using Eq. (19), Eq. (22) simplifies to

$$\Big\langle |f_{lm}|^2 \Big\rangle = e^{-2t/\tau_l}|f_{lm}(0)|^2 + \frac{2\mathrm{k}_B T\Gamma_l}{\eta_{\mathrm{ex}} R_0^3}\int_0^t e^{-2(t-t')/\tau_l}dt'. \tag{23}$$

$$\Big\langle |f_{lm}|^2 \Big\rangle = e^{-2t/\tau_l}|f_{lm}(0)|^2 + \frac{\mathrm{k}_B T\Gamma_l\tau_l}{\eta_{\mathrm{ex}} R_0^3}\Big[1 - e^{-2t/\tau_l}\Big] \tag{24}$$

At long times, $t >> \tau_l$, Eq. (24) simplifies to

$$\Big\langle |f_{lm}|^2 \Big\rangle = \frac{\mathrm{k}_B T\Gamma_l\tau_l}{\eta_{\mathrm{ex}} R_0^3} = \frac{k_B T}{\kappa}\left[(l+2)(l-1)\Big(l(l+1) + \bar{\sigma}\Big)\right]^{-1} \tag{25}$$

Recall $\bar{\sigma} = \sigma R_0^2/\kappa$. Since the dynamics of the different spherical harmonics modes are completely decoupled, we can more generally say

$$\Big\langle f^*_{lm} f_{l'm'} \Big\rangle = \frac{k_B T\Gamma_l\tau_l}{\eta_{\mathrm{ex}} R_0^3} = \frac{k_B T}{\kappa}\left[(l+2)(l-1)\Big(l(l+1)\kappa + \bar{\sigma}\Big)\right]^{-1}\delta_{ll'}\delta_{mm'} \tag{26}$$

Next, we consider the contour of the GUV at the equator as a function of the spherical harmonic coefficients:

$$r(\phi,t) = R_0\left(1 + \sum_{q=0}^{q_{\max}} u_q(t)e^{\mathrm{i}q\phi}\right) = R_0\Big(1 + \sum_{l=0}^{l_{\max}}\sum_{m=-l}^{l} f_{lm}(t)\mathcal{Y}_{lm}(\pi/2,\phi)\Big). \tag{27}$$

The Fourier coefficient for the q-th mode is then given by

$$u_q(t) = \frac{1}{2\pi R_0}\int_0^{2\pi} r(\phi,t)e^{-iq\phi}d\phi = \sum_{l=q}^{l_{\max}} f_{lq}(t)\left(n_{lq}P_{lq}(0)e^{\mathrm{i}q\phi}\right)e^{-\mathrm{i}q\phi} \tag{28}$$

as all the other terms integrate to zero. In the above equation, we have inserted the definition of the spherical harmonic, $\mathcal{Y}(\theta,\phi) = n_{lm}P_{lm}(\cos\theta)e^{\mathrm{i}m\phi}$ (see Eq.(5)), which shows that the dependence on ϕ cancels out.

The mean squared amplitude of u_q is then given by

$$\big\langle |u_q|^2 \big\rangle = \sum_{l=q}^{l_{\max}}\sum_{l'=q}^{l_{\max}} \big\langle f^*_{l'q} f_{lq}\big\rangle n_{lq}n_{l'q}P_{lq}(0)P^*_{l'q}(0). \tag{29}$$

Using Eq. (26), the above equation simplifies to

$$\left\langle |u_q|^2 \right\rangle = \sum_{l=q}^{l_{\max}} \left\langle |f_{lq}|^2 \right\rangle n_{lq}^2 |P_{lq}(0)|^2 \tag{30}$$

$$\left\langle |u_q|^2 \right\rangle = \mathrm{k}_B T \sum_{l=q}^{l_{\max}} \left[(l+2)(l-1)\Big(l(l+1)\kappa + \sigma R_0^2 \Big) \right]^{-1} n_{lq}^2 |P_{lq}(0)|^2 \tag{31}$$

Eq.(31) follows q^{-3} behavior for bending dominated modes $q > \sqrt{\bar{\sigma}}$ (and q^{-1} behavior for tension dominated modes $q < \sqrt{\bar{\sigma}}$).

Time Correlation for Fourier Modes: Time correlations present another useful metric to analyze the membrane fluctuations. As the different spherical harmonics modes are independent, the average time correlations,

$$\Big\langle u_q(0) u_q^*(t) \Big\rangle = \sum_{l'=|q|}^{l_{max}} \sum_{l''=|q|}^{l_{max}} \Big\langle f_{l'q}(0)\ f_{l''q}^*(t) \Big\rangle n_{l'q} n_{l''q} P_{l'q}(0)\ P_{l''q}^*(0), \tag{32}$$

can be simplified to

$$\Big\langle u_q(0) u_q^*(t) \Big\rangle = \sum_{l=|q|}^{l_{max}} \Big\langle f_{lq}(0)\ f_{lq}^*(t) \Big\rangle n_{lq}^2 \Big| P_{lq}(0) \Big|^2 , \tag{33}$$

Using (21), (32) can be rewritten as

$$\Big\langle u_q(0) u_q^*(t) \Big\rangle = \sum_{l=|q|}^{l_{max}} \Big\langle |f_{lq}|^2 \Big\rangle n_{lq}^2 \Big| P_{lq}(0) \Big|^2 e^{-t/\tau_l}. \tag{34}$$

Since the first term in (34) has both the smallest decay rate (τ_q^{-1}) and largest mean-squared amplitude, the time correlation can be approximated to leading order as

$$\Big\langle u_q(0) u_q^*(t) \Big\rangle = \Big\langle |f_{qq}|^2 \Big\rangle n_{qq}^2 \Big| P_{qq}(0) \Big|^2 e^{-t/\tau_q}. \tag{35}$$

If we consider limit of undulations with short wavelengths (shorter than the vesicle radius), $q \gg 1$, then the leading order decay rate can be approximated as

$$\tau_q^{-1} \approx \frac{q^3 R_0^{-3} \kappa + q R_0^{-1} \sigma}{2(\eta_{\mathrm{ex}} + \eta_{\mathrm{in}})} = \frac{\kappa}{\eta_{\mathrm{ex}} R_0^3} \frac{q^3 + q\bar{\sigma}}{2(1+\lambda)} \tag{36}$$

which is the decay rate derived using planar fluctuations. However, we suggest using the exact decay rate from the spherical harmonics as it is both more accurate and valid for all Fourier modes.

When comparing the time correlations in Fig.7, the exact decay rate, from the full spherical harmonics (SpH), is immediately more accurate than if the planar membrane (PM) decay rate is used. To get the accuracy even better, the higher order terms in Eq. (34) must be included. If all of the terms are included then the time correlation is directly on top of the curve from produced by the numerical simulation. However, as it is not feasible to include all the terms for real membranes, it is of interest to know how many terms are enough to sufficiently reproduce the numerical simulations. As shown in Figure 5, the time correlation produced by including the first two terms in Eq. (34 lies almost directly on top of the true solution. Including more terms would improve the accuracy further, but it is not likely to be significant due to experimental error.

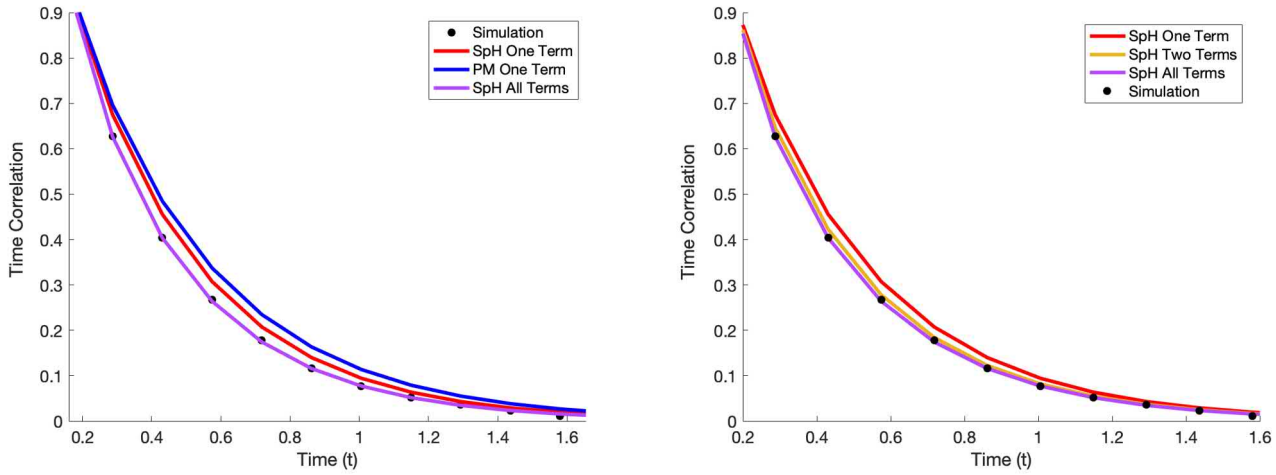

Fig. S 7: Plots comparing the analytic approximations for time correlation for Fourier mode $q = 5$. The left plots the time correlations using the exact spherical harmonic (SpH) decay rate and the less accurate planar membrane (PM) decay rate. The right plots the time correlations for the SpH case using different number of terms. The black dots show the time correlations computed from a numerical simulation using the following parameters as inputs. $R_0 = 3\times10^{-5}$ m, $\kappa = 5\times10^{-19}$ J, $\sigma = 4\times10^{-8}$ N/m, $l_{max} = 14$

Cross-Spectral Density: Similar to time correlations, the Cross-Spectral Density (CSD) is given by

$$\Big\langle |u_q(0)||u_q(t)| \Big\rangle - \Big\langle |u_q|^2(0) \Big\rangle. \tag{37}$$

For the sake of clarity of explanation, in this section we will use the leading order approximation of u_q,

$$u_q(t) \approx f_{qq}(t) n_{qq} P_q \left(\cos\frac{\pi}{2}\right). \tag{38}$$

Using (20), this can be rewritten as

$$u_q(t) = e^{-t/\tau_l} u_q(0) + \bar{\zeta}_q(t), \tag{39}$$

where

$$\bar{\zeta}_q = n_{qq} P_{qq}(0) \int_0^t e^{-(t-t')/\tau_l} \zeta_{lm}(t') dt'$$

is a random normally distributed Weiner process.

From (39), it is clear that $u_q(t) = \bar{\zeta}_q(t)$ for large values of t. Furthermore, it is worth noting that all Fourier modes, except $q = 0$, have both real and an imaginary component, $u_q = A_q + \mathrm{i}B_q$, and that these two components are independent of each other. Likewise, the thermal noise can be decomposed into independent real and imaginary components: $\bar{\zeta}_q = \bar{\zeta}_{Aq} + \mathrm{i}\bar{\zeta}_{Bq}$. The real component of Eq. (39) can then be written as

$$A_q(t) = A_q(0) e^{-t/\tau_q} + \bar{\zeta}_{Aq}(t) \tag{40}$$

and a similar expression for B_q.

Therefore, it can be shown that

$$\begin{aligned}\Big\langle |u_q(0)||u_q(t)| \Big\rangle &= \Big\langle |u_q(0)| \Big(A_q^2(t) + B_q^2(t) \Big)^{1/2} \Big\rangle \\ &= \Big\langle |u_q(0)| \Big(|\bar{\zeta}_q|^2(t) + 2\big(\bar{\zeta}_{Aq}(t) A_q(0) + \bar{\zeta}_{Bq}(t) B_q(0)\big) e^{-t/\tau_q} + |u_q(0)|^2 e^{-2t/\tau_q} \Big)^{1/2} \Big\rangle \end{aligned} \tag{41}$$

If we assume that $t >> t_q$, then we can perform the following expansion

$$\begin{aligned}\Big\langle |u_q(0)||u_q(t)| \Big\rangle = \Big\langle |u_q(0)| \Big\rangle \Big\langle |\bar{\zeta}_q(t)| \Big\rangle \\ + \left(\Big\langle |u_q(0)| A_q(0) \Big\rangle \Big\langle \frac{\bar{\zeta}_{Aq}(t)}{|\bar{\zeta}_q(t)|} \Big\rangle + \Big\langle |u_q(0)| B_q(0) \Big\rangle \Big\langle \frac{\bar{\zeta}_{Bq}(t)}{|\bar{\zeta}_q(t)|} \Big\rangle \right) e^{-t/\tau_q} \\ + \frac{1}{2} \left(\frac{\Big\langle |u_q(0)|^3 \Big\rangle}{\Big\langle |\bar{\zeta}_q(t)| \Big\rangle} - \Big\langle \frac{|u_q(0)| \big(\bar{\zeta}_{Aq}(t) A_q(0) + \bar{\zeta}_{Bq}(t) B_q(0) \big)^2}{|\bar{\zeta}_q(t)|^3} \Big\rangle \right) e^{-2t/\tau_q} + \mathcal{O}\big(e^{-3t/\tau_q}\big). \end{aligned} \quad (42)$$

The second term in (42) averages to zero due to the thermal noise factor. Therefore, to leading order, the CSD is given as

$$\Big\langle |u_q(0)||u_q(t)| \Big\rangle - \Big\langle |u_q(0)| \Big\rangle^2 = C_q e^{-2t/\tau_q} + \mathcal{O}\big(e^{-3t/\tau_q}\big) \quad (43)$$

where C_q is a normalization constant.

Therefore, the slowest decaying mode of the CSD is $\mathcal{O}\big(e^{-2t/\tau_q}\big)$. This contradicts H. Zhou et al. [11] who give it as $\mathcal{O}\big(e^{-t/\tau_q}\big)$. This factor of two is a consequence that each Fourier coefficient has both a real and imaginary component that are completely independent of each other.

Finally, users are recommended to use time correlations over CSD. CSD requires the same amount of work and contains the same higher order error as the time correlation method. Yet, CSD has an additional layer of truncation error introduced in the expansion in Eq.(42).

Movie S1

Real-time video of the GUV from Figure 1 in the main text (DOPC labeled with 0.2 mol % TR-DHPE) acquired with phase contrast microscopy. The vesicle radius is 29.6 μm.

Movie 2

Video of the GUV from Figure 1 in the main text (DOPC labeled with 0.2 mol % TR-DHPE) acquired with confocal microscopy. The objective used is 40x/0.6 NA with the pinhole size 1 A.U. The polarization effect was corrected by using circular rotation plates to have even intensities across the equatorial vesicle plane. The vesicle radius is 29.6 μm.

Movie S3

Real time video of the GUV from Figure 6 in the main text consisting of DOPC labeled with TR DHPE (0.8%) acquired with confocal microscopy. The objective used is 40x/0.6 NA at 13.2 fps with the pinhole size 1 A.U. The polarization effect was corrected by using circular rotation plates to have even intensities across the equatorial vesicle plane.

Raw data

Raw data are available at `https://dx.doi.org/10.17617/3.4p`. This collection of raw data, consists of 4 folders each containing zipped files of data.

In folder "Raw data - Fourier modes", 2 different sets of experimental data are included: phase contrast (PC) and confocal (C) microscopy on the same vesicle and confocal microscopy data with different pinhole sizes. The folder contains excel sheets with fluctuation amplitude for every Fourier mode and the metadata with all the microscopy conditions. The vesicles have different sizes so that they practically cover a good span of focal depth (Δ) from 0.03 to 0.15. The meta data is included in the first sheet of the excel file. The second sheet has the mode and mean squared amplitude (and error). The remaining sheets have the Fourier modes for every microscopy setting (and focal depth). Note that our Fourier signal was normalized by vesicle radius. For the definition of our Fourier transform, please refer to *Gracia et al.*[3]. The contour detection is conducted as given in the main text and supplement.

The rest of the folders as listed below contain vesicle images in tiff format (grouped in folders for the separate vesicle as suggested by the folder name) and an excel sheet with the meta data indicating the specific microscopy conditions (AU = Airy unit, NA = numerical aperture).

The folder "Raw images - different focal depth" contains confocal microscopy raw images at different focal depths without any image processing for vesicles of different sizes.

The folder "Raw images - phase contrast vs confocal" contains phase contrast and confocal microscopy raw images for the same vesicle without any image processing for vesicles of different sizes.

The folder "Raw images - polarization correction" contains polarized and polarization-corrected confocal microscopy raw images for the same vesicle without any image processing.

[1] R. Dimova. Recent developments in the field of bending rigidity measurements on membranes. Adv. Coll. Int. Sci., 208:225–234, 2014.

[2] Joanna B. Dahl, Vivek Narsimhan, Bernardo Gouveia, Sanjay Kumar, Eric S. G. Shaqfeh, and Susan J. Muller. Experimental observation of the asymmetric instability of intermediate-reduced-volume vesicles in extensional flow. Soft Matter, 12:3787–3796, 2016.

[3] R. S. Gracia, N. Bezlyepkina, R. L. Knorr, R. L. Lipowsky, and R. Dimova. Effect of cholesterol on the rigidity of saturated and unsaturated membranes: fluctuation and electrodeformation analysis of giant vesicles. Soft Matter, 6:1472-1482, 2010.

[4] Yuval Elani, Sowmya Purushothaman, Paula J. Booth, John M. Seddon, Nicholas J. Brooks, Robert V. Law, and Oscar Ces. Measurements of the effect of membrane asymmetry on the mechanical properties of lipid bilayers. Chem. Commun., 51:6976–6979, 2015.

[5] Dinesh Kumar, Channing M. Richter, and Charles M. Schroeder. Conformational dynamics and phase behavior of lipid vesicles in a precisely controlled extensional flow. Soft Matter, 16:337–347, 2020.

[6] Aidan T. Brown, Jurij Kotar, and Pietro Cicuta. Active rheology of phospholipid vesicles. Phys. Rev. E, 84:021930, Aug 2011.

[7] Arwen I. I. Tyler, Jake L. Greenfield, John M. Seddon, Nicholas J. Brooks, and Sowmya Purushothaman. Coupling phase behavior of fatty acid containing membranes to membrane bio-mechanics. Frontiers in Cell and Developmental Biology, 7:187, 2019.

[8] Sowmya Purushothaman, Pietro Cicuta, Oscar Ces, and Nicholas J. Brooks. Influence of high pressure on the bending rigidity of model membranes. The Journal of Physical Chemistry B, 119(30):9805–9810, Jul 2015.

[9] P Shchelokovskyy, S Tristram-Nagle, and R Dimova. Effect of the HIV-1 fusion peptide on the mechanical properties and leaflet coupling of lipid bilayers. New Journal of Physics, 13(2):025004, feb 2011.

[10] S. Alex Rautu, Davide Orsi Lorenzo Di Michele, George Rowlands Pietro Cicuta and Matthew S. Turner. The role of optical projection in the analysis of membrane fluctuations. Soft. Matter., 17, 2017 3480-3483.

[11] H. Zhou, B. B. Gabilondo, W. Losert, and W. van de Wate. Stretching and relaxation of vesicles. Phys. Rev. E, 83:011905, 2011.

[12] W. Rawicz, K.C. Olbrich, T. McIntosh, D. Needham, and E. Evans. Effect of chain length and unsaturation on elasticity of lipid bilayers. Biophys. J., 79:328–339, 2000.

[13] Jianjun Pan, Stephanie Tristram-Nagle, Norbert Kučerka, and John F. Nagle. Temperature dependence of structure, bending rigidity, and bilayer interactions of dioleoylphosphatidylcholine bilayers. Biophysical Journal, 94(1):117–124, Jan 2008.

[14] M. S. Jablin, K. Akabori, and J. F. Nagle. Experimental support for tilt-dependent theory of biomembrane mechanics. Phys. Rev. Lett., 113:248102, Dec 2014.

[15] B. Sorre, A. Callan-Jones, J.-B. Manneville, P. Nassoy, J.-F. Joanny, J. Prost, B. Goud, and P. Bassereau. Curvature-driven lipid sorting needs proximity to a demixing point and is aided by proteins. PNAS, 106:5622–5626, 2009.

[16] Sudipta Gupta, Judith U. De Mel, Rasangi M. Perera, Piotr Zolnierczuk, Markus Bleuel, Antonio Faraone, and Gerald J. Schneider. Dynamics of phospholipid membranes beyond thermal undulations. The Journal of Physical Chemistry Letters, 9(11):2956–2960, Jun 2018.

[17] Judith U. De Mel, Sudipta Gupta, Rasangi M. Perera, Ly Ngo, Piotr Zolnierczuk, Markus Bleuel, Sai Venkatesh Pingali, and Gerald J. Schneider. Influence of salt on membrane rigidity of neutral DOPC vesicles. Langmuir, 36:9356–9367, 2020.

[18] T. Betz, and C. Sykes. Time resolved membrane fluctuation spectroscopy. Soft. Matter., 8, 2012 5317-5326.

[19] Miglena I. Angelova and Dimiter S. Dimitrov. Liposome electroformation. Faraday Discuss. Chem. Soc., 81:303–311, 1986.

[20] K. K. Scott E. Maxwell, Harold D. Delaney, Designing Experiments and Analyzing Data: A Model Comparison Perspective, Taylor and Francis, 3rd edn., 2017

[21] Michael Chernick. Bootstrap Methods: A Guide for Practitioners and Researchers. John Wiley & Sons, Inc., 2 edition, 2007.

[22] U. Seifert. Configurations of fluid membranes and vesicles. Advances in physics, 46:13–137, 1997.

[23] U. Seifert. Fluid membranes in hydrodynamic flow fields: Formalism and an application to fluctuating quasispherical vesicles. Eur. Phys. J. B, 8:405–415, 1999.

[24] P. M. Vlahovska. Dynamics of membrane bound particles: capsules and vesicles. In C. Duprat and H.A. Stone, editors, Low-Reynolds-Number Flows: Fluid-Structure Interactions. Royal Society of Chemistry Series RSC Soft Matter, 2016.

[25] Petia M. Vlahovska and C. Misbah. Theory of vesicle dynamics in flow and electric fields. In R. Dimova and C. Marques, editors, The Giant Vesicle Book, page Chapter 7. CRC Press, 2019.

[26] S. T. Milner and S. A. Safran. Dynamical fluctuations of droplet microemulsions and vesicles. Phys. Rev. A, 36:4371–4379, 1987.

[27] D. Gillespie. Exact numerical simulation of the Ornstein-Uhlenbeck process and its integral. Physical Review E, 54, 1996 2084-2091.